



1 **Microphysical characteristics of precipitation within**  
2 **convective overshooting over East China observed by**  
3 **GPM DPR and ERA5**

4 Nan Sun<sup>1</sup>, Gaopeng Lu<sup>1</sup>, Yunfei Fu<sup>1</sup>

5 <sup>1</sup>School of Earth and Space Sciences, University of Science and Technology of China, Hefei, 230026,  
6 China

7 *Corresponding to:* Yunfei Fu, fyf@ustc.edu.cn

8 **Abstract.** We examine geographical distribution pattern of convective overshooting and its internal  
9 microphysical three-dimensional structure of precipitation over East China by matching Global  
10 Precipitation Measurement Dual-frequency Precipitation Radar instrument (GPM DPR) with European  
11 Centre for Medium-Range Weather Forecasts 5th Reanalysis (ERA5). Convective overshooting events  
12 mainly occur over NC (Northeast China) and northern MEC (Middle and East China), with a magnitude  
13 of only  $10^{-3}$ ; Radar reflectivity of convective overshooting over NC accounts for a higher proportion  
14 below the zero level, while MEC and SC (South China) account for a higher proportion above the zero  
15 level, indicating stronger upward motion and more ice crystal particles; The microphysical processes  
16 within convective overshooting are unique, leading to various properties of the droplets in precipitation.  
17 Droplets of convective overshooting are large, but sparse. And its effective radius of droplet, below 10  
18 km altitude, is almost exceeding 2.5 mm, which is about twice than normal precipitation. Convective  
19 overshooting humidifies air below the cloud top and obviously increases the ozone near tropopause as a  
20 result of influx of ozone from lower troposphere and sinking of air with high concentration ozone in the  
21 stratosphere. Findings of this study may have important implications for the microphysical evolution  
22 associated with convective overshooting, and provide more accurate precipitation microphysical  
23 parameters as the input of the model simulation.

24

25



## 26 **1 Introduction**

27 Convective overshooting provides a rapid transport mechanism that can irreversibly transport water  
28 vapor and chemical constituents from lower troposphere to the upper troposphere and lower stratosphere  
29 (UTLS) by mixing them with environmental air (Fueglistaler et al., 2004; Frey et al., 2015), which has a  
30 direct impact on radiation balance and global climate change (Solomon et al., 2010). As one of the main  
31 sources of ozone destroying OH hydroxyl radicals, stratospheric water vapor can help to destroy ozone,  
32 which has potential effects on radiative forcing (Anderson et al., 2012). Previous studies show that  
33 convective overshooting has a net dehydrating effect on the stratospheric humidity (Danielsen, 1993;  
34 Sherwood and Dessler, 2001). Recently, modeling and observational studies show the moistening effect  
35 of convective overshooting on the stratosphere (Chaboureau et al. 2007; Jensen et al. 2007; de Reus et al.  
36 2009; Avery et al. 2017) because of the injection of ice mass into the stratosphere (Grosvenor et al., 2007;  
37 Corti et al., 2008; Chemel et al., 2009; Khaykin et al., 2009). In addition to these impacts on water vapor,  
38 the convective overshooting affecting on the UTLS temperature has also attracted much attention  
39 (Sherwood et al., 2003; Chae et al., 2011; Biondi et al., 2012).

40 In addition to UTLS composition effects, convective overshooting is often associated with severe and  
41 hazardous weather (e.g., heavy rain, hail, tornadoes, and strong winds) at the Earth's surface with  
42 important impacts on society and economy (Line et al., 2016; Bedka et al., 2018; Marion et al., 2019).  
43 Given these potentially significant impacts, it's of high importance to understand the characteristics of  
44 convective overshooting, which attract considerable attention in recent years (Johnston et al., 2018;  
45 Muhsin et al., 2018).

46 Perhaps one of the most poorly understood features of convective overshooting is the microphysical  
47 structure of precipitation, such as particle size, concentration, phase state and other parameters.  
48 Understanding the microphysical characteristics of convective overshooting is helpful to clarify the  
49 efficiency of water vapor transported to the lower stratosphere by convective overshooting. In addition,  
50 the microphysical processes within convective overshooting are closely related to storm dynamics and  
51 thermodynamics through latent heat, and the quantitative description of microphysical characteristics is  
52 helpful to improve the accuracy of model simulation parameters (Homeyer and Kumjian, 2015). Liu et al.  
53 (2012) studied the climatological characteristics of convective overshooting and found that rain rates of  
54 convective overshooting are bigger than that of deep convection. Homeyer and Kumjian (2015) observed



55 the radar reflectivity characteristics within the convective overshooting from the analysis of the  
56 polarimetric radar. Although the above studies have explored the characteristics of some precipitation  
57 parameters within convective overshooting, we still lack the understanding of more precipitation  
58 microphysical parameters and more detailed microphysical processes within convective overshooting  
59 due to the limitations of observation methods.

60 To fully study the microphysical characteristics of convective overshooting, accurate methods of  
61 detecting the frequency and long-term distribution of convective overshooting are required. The  
62 traditional ways for detecting convective overshooting is to find pixels with brightness temperatures  
63 colder than a given temperature threshold (Machado et al. 1998; Rossow and Pearl 2007). Gettelman et al.  
64 (2002) have studied the cloud regions colder than the tropopause temperature on infrared images and  
65 found that the frequency of tropical convective overshooting is about 0.5%. However, it is impossible to  
66 guarantee that the low value of infrared brightness temperature represents clouds penetrating the  
67 tropopause rather than cirrus or cloud anvil in the upper air due to the lack of vertical structure  
68 information of convection. With the launch of Precipitation Radar aboard Tropical Rainfall Measuring  
69 Mission (TRMM), three-dimensional structure information of precipitation within the convective  
70 overshooting can be provided (Alcala and Dessler, 2002; Liu and Zipser, 2005) and a new method for  
71 detecting the convective overshooting is proposed that is to find pixels with rain top height higher than  
72 tropopause height (Xian and Fu, 2015; Sun et al., 2021), which improve the accuracy of detecting  
73 convective overshooting. Still, TRMM PR can't provide the precipitation microphysical information,  
74 which limits our study on the internal microphysical structure within convective overshooting. Besides,  
75 TRMM PR can underestimate the height of convective overshooting because of only sensitive to large  
76 precipitation particles (sensitivity at ~17 dBZ) (Hanii and Zheng, 2014).

77 As the continuation of TRMM PR, Global Precipitation Measurement (GPM) carrying the first  
78 Dual-frequency Precipitation Radar (DPR) launched in February 2014. GPM DPR include two bands of  
79 precipitation radar, which provides excellent opportunities for studying the microphysical structure of  
80 precipitation (Sun et al., 2022a). Liu et al., (2016, 2019) have used GPM KuPR and ERA-Interim  
81 6-hourly data set to study climatology and detection of convective overshooting. However, the above  
82 studies only use the KuPR data and mainly focus on the geographical distribution, the microphysical  
83 processes of convective overshooting remain unknown. Besides, the matching time between GPM and  
84 ERA-Interim is too long (6 hour) to ensure the accuracy of convective overshooting detection.



85 Another difficulty in convective overshooting detection is to obtain tropopause height data with high  
86 spatial and temporal resolution. On the one hand, the determination of the tropopause is still under debate.  
87 At present, the following two definitions of the tropopause are widely adopted throughout the world: one  
88 is the cold tropopause, and the other is the thermodynamic tropopause. However, the cold point  
89 tropopause is only physically meaningful in the latitude zone 10°S-10°N near the equator (Highwood  
90 and Hoskins, 1998; Rodriguez-Franco and Cuevas, 2013). Therefore, this paper uses the thermodynamic  
91 tropopause, which is defined by the World Meteorological Organization (WMO) (WMO, 1957). The  
92 thermodynamic tropopause is based on the temperature lapse rate, also known as lapse-rate tropopause.  
93 The accurate calculation of the tropopause height based on this definition, on the other hand, depends on  
94 the temperature profile data with high spatial and temporal resolution. The latest generation of reanalysis  
95 data ERA5 provides hourly estimates of a large number of atmospheric, land and oceanic climate  
96 variables, which has attracted much attention due to its much higher spatial and temporal resolution than  
97 its predecessor ERA-Interim, especially in the upper troposphere and lower stratosphere (Hoffmann et al.  
98 2019). Sun et al. (2022b) verified the accuracy for the tropopause height calculated from temperature  
99 profiles of ERA5 by comparing ERA5 with other popular datasets.

100 East China is located in the East Asian monsoon region, with unique climate characteristics. The  
101 precipitation of East China in summer is affected by the circulation anomalies of the East Asian tropical  
102 and subtropical monsoon and their interactions. The precipitation anomalies not only have an important  
103 impact on industrial and agricultural production, social infrastructure construction, but also threaten the  
104 safety of human life and property. Many scholars have studied the characteristics of precipitation in East  
105 China (Zhang et al., 2018; Xu, 2020), but few have studied the characteristics of convective overshooting  
106 and its internal precipitation microphysical structure over East China. The purpose of this study is to  
107 examine the microphysical characteristics of convective overshooting over East China by matching the  
108 precipitation data from GPM DPR and meteorological parameters from ERA5.

## 109 **2 Data and method**

### 110 **2.1 DPR-based precipitation dataset**

111 GPM DPR include KuPR (Ku band, 13.6 GHz) and KaPR (Ka band, 35.5 GHz), two bands of  
112 precipitation radar. KuPR is similar to TRMM PR and has a longer wavelength, which is better at



113 detecting heavy precipitation (the minimum detected precipitation is about 0.5 mm/h). However, KaPR  
114 has a shorter wavelength, which is more sensitive to weak precipitation (the minimum detected  
115 precipitation is about 0.2 mm/h). Based on the different echo characteristics of Ku band and Ka band, the  
116 dual channel inversion algorithm can be used to retrieve DSD (Droplet Size Distribution). Here we use  
117 the precipitation datasets are provided by the GPM level 2 product 2ADPR in version 6 from 2014 to  
118 2020 in summer (June, July and August). The horizontal resolution is 5 km and the vertical resolution is  
119 125m. The precipitation microphysical parameters provided by GPM 2ADPR include droplet  
120 concentration ( $dB N_0$ ) and effective radius ( $D_0$ ).

## 121 **2.2 ERA5-based meteorological dataset**

122 The meteorological data are from ERA5 reanalysis datasets. And the following parameters are used in  
123 this paper: temperature, specific humidity, vertical velocity, ozone mass mixing ratio, U-component of  
124 wind, and V-component of wind. The time resolution is 1 h and the horizontal resolution is  $0.25^\circ \times 0.25^\circ$ .

## 125 **2.3 Definition of the convective overshooting**

126 The convective overshooting is defined as the storm top height above the real-time tropopause height.  
127 storm top height is obtained from the GPM DPR. Tropopause height is calculated from the temperature  
128 profiles from ERA5 according to the definition from the World Meteorological Organization, whose  
129 characteristics are as follow: (1) the atmospheric lapse rate is  $2 \text{ K km}^{-1}$  or less and (2) the atmospheric  
130 lapse rate does not exceed  $2 \text{ K km}^{-1}$  between the tropopause level and all higher levels within 2 km  
131 (WMO, 1957).

## 132 **2.4 Study areas**

133 The study areas are marked as black boxes in Fig. 1a and only the land parts are studied. To have a better  
134 understanding of precipitation microphysical structure over different regions of East China, we divided  
135 the study areas into three parts according to its climatic characteristics and previous studies (Sun et al.,  
136 2022a). From north to south, they are NC (Northeast China;  $38^\circ\text{--}50^\circ \text{N}$ ,  $118^\circ\text{--}130^\circ \text{E}$ ), MEC (Middle and  
137 East China;  $26.5^\circ\text{--}38^\circ \text{N}$ ,  $112^\circ\text{--}123^\circ \text{E}$ ), and SC (South China;  $18^\circ\text{--}26.5^\circ \text{N}$ ,  $108^\circ\text{--}123^\circ \text{E}$ ).



138 **3 Results**

139 **3.1 Case studies**

140 Three cases selected from NC, MEC and SC are analyzed to lay a foundation for the subsequent  
141 statistical analysis. The precipitation characteristics of the three cases are shown as Fig. 2. The Case 1  
142 (C1) occurs in NC. A total of 65 pixels in which convective overshooting occurs and their rain rate are  
143 mostly over 20 mm/h (Fig. 2a) and their storm top height are over 12 km (Fig. 2b). The strong radar  
144 reflectivity along A1B1 occurs at 35-95km away from point A1, and the strongest echo is up to 50 dBZ,  
145 appears at 0-5 km (Fig. 2c). The maximum echo height is about 15 km, 2 km higher than the tropopause  
146 height. The Case 2 (C2) occurs in MEC. There are 58 pixels in which convective overshooting occurs  
147 and their rain rate are more than 25 mm/h (Fig. 2d) and their storm top height are mostly over 14 km (Fig.  
148 2e). The radar echo along A2B2 is very strong and the strongest echo is up to 50 dBZ, which is about  
149 45-95 km away from point A2 (Fig. 2f). The highest echo can reach to about 17 km altitude. The Case 3  
150 (C3) occurs in SC. There are 8 convective overshooting pixels in C3 and their rain rate is over 20 mm/h  
151 (Fig. 2g) and their storm top height is between 14 and 18 km (Fig. 2h). The strongest echo occurs at 60-70  
152 km away from point A3 and the highest echo can reach to 17.2 km, about 0.5 km higher than the  
153 tropopause height (Fig. 2i).

154 To learn about the characteristics of large scale circulation of cases, we calculate the distribution of  
155 Precipitable Water Vapor (PWV), streamlines and Vertical Velocity (VV), shown as Fig. 3. In general,  
156 the area in which convective overshooting occurs have abundant PWV and strong ascending movement.  
157 In C1, PWV is between 20 and 65 mm. The PWV of the area where the precipitation case occurs (big  
158 black box) is between 40 and 55 mm. The PWV of the region in which convective overshooting occurs is  
159 obviously higher than else region, which is between 50 and 55 mm (Fig. 3a). The vertical upward  
160 movement near the convective overshooting is strong, range between -0.03 and -0.12 Pa/s (Fig. 3b). In  
161 C2, The PWV of the area where the precipitation case occurs is between 50 and 65mm. The PWV of the  
162 area in which convective overshooting occurs are between 50 and 55 mm (Fig. 3c). The VV near the  
163 convective overshooting is mostly between -0.09 and -0.15 Pa/s (Fig. 3d). In C3, the PWV near the  
164 precipitation area and convective overshooting area are both between 65 and 75 mm (Fig. 3e), which are  
165 relatively high. The vertical upward movement near the precipitation area and convective overshooting  
166 area are very strong and the VV are between -0.12 and -0.18 Pa/s.



167 **3.2 Statistical results**

168 **3.2.1 Geographical distribution**

169 Firstly, the horizontal distribution characteristics of convective overshooting over East China are  
170 analysed by designing a more accurate algorithm for convective overshooting determination. Accurate  
171 determination of tropopause height is the first step of the convective overshooting determination  
172 algorithm. We first analyze geographical distribution of tropopause over East China calculated from  
173 ERA5, shown as Fig. 1b. In general, the tropopause height over East China is between 11.6 km and 16.7  
174 km and has an obvious zonal distribution pattern: Tropopause height over SC and southern MEC  
175 (18-36 °N) is the highest and has small spatial variabilities, concentrated at ~16.7 km. Over northern  
176 MEC (36-38 °N), tropopause height obviously decreases and forms a gradient, which decreases to 16 km.  
177 Tropopause height over NC is the smallest and continues to decrease in a gradient pattern from south to  
178 north, decreasing to 13 km near central NC (45 °N) and 12 km near northern NC (48 °N). Minimum  
179 standard deviation of tropopause height appears in SC, along with central and southern MEC, lower than  
180 0.2 km. From northern MEC to northern NC, the standard deviation first increases and then decreases,  
181 reaching a maximum of more than 2 km around 42 °N, and standard deviation over NC is generally above  
182 1 km.

183 Obtaining storm top height from precipitation data is the second step of convective overshooting  
184 algorithm. Fig. 4 show geographical distribution of storm top height for total precipitation, convective  
185 precipitation and convective overshooting. As shown, mean storm top height over East China vary from  
186 4.5 km to 8.5 km, while convective storm top height is mainly distributed between 3.5 km and 9 km.  
187 Convective storm top height over NC and northern MEC are the highest, with most areas exceeding 6.5  
188 km and as we noted above, tropopause height in these two regions are lower (Fig. 1b), it can be inferred  
189 that convective overshooting events are more likely to occur. Further analysis of the frequency of  
190 convective overshooting in the following text will confirm this point. Compared with NC, convective  
191 storm top height over SC and southern MEC is lower, mainly distributed below 6.5 km. Storm top height  
192 of convective overshooting range from 10 km to 21 km (Fig. 4c), obviously much higher than normal  
193 precipitation (total and convective precipitation) and increasing gradually from north to south. Storm top  
194 height of convective overshooting over NC and northern MEC are low, distributed between 10 km and  
195 16 km, which is because that their lower tropopause height (Fig. 1b) allow convection with lower storm



196 top height to penetrate troposphere, lowering the mean storm top height of convective overshooting,  
197 while that over SC and southern MEC range from 16 km to 21 km, with higher tropopause height (Fig.  
198 1b), allowing only stronger convection to penetrate the troposphere.

199 Based on the tropopause and storm top height information calculated above, algorithm for convective  
200 overshooting determination over East China is designed and its geographical distribution of sample size  
201 and frequency are shown as Table 1 and Fig. 5. The frequency of convective overshooting is defined as  
202 the number of convective overshooting events divided by the total observed sample number of GPM  
203 DPR. Statistical results indicate that the frequency of the convective overshooting over East China is  
204 very low, with a magnitude of only  $10^{-3}$ , with regionally different. NC has the highest frequency of  
205 convective overshooting, with sample size of 2394 (count, ct), followed by MEC with 582 ct, and SC is  
206 the lowest (296 ct). Convective overshooting over NC and northern MEC, whose frequency range from  
207  $4 \times 10^{-4}$  to  $5.4 \times 10^{-3}$ , occur more frequently than SC and southern MEC, whose frequency is between  
208  $2 \times 10^{-4}$  and  $6 \times 10^{-4}$ , which is mainly because the former has a lower tropopause height and it's easier for  
209 convective overshooting to occur.

### 210 3.2.2 Vertical structures

211 Based on the reflectivity profiles and the rain-rate profiles provided by the GPM DPR instrument, we  
212 studied the vertical structure of precipitation within convective overshooting. DPDH (Distribution of  
213 Probability Density with Height) analysis of radar reflectivity can effectively indicate the  
214 three-dimensional structure characteristics of precipitation, which is therefore applied in a large number  
215 of precipitation studies (Yuter and Houze, 1995). Fig. 6 shows DPDH of the DPR radar reflectivity. In  
216 general, radar reflectivity within convective overshooting is obviously stronger and its storm top height  
217 is higher. And the DPDH analysis also shows obviously regional differences. Radar echo intensity of  
218 convective overshooting over NC is the weakest, and the echo near surface is mainly distributed from 25  
219 dBZ to 55 dBZ, with sharp peak 47 dBZ, while the peak of the total precipitation is around 16 dBZ. And  
220 the max radar echo top within convective overshooting over NC can reach to 13.5 km, 3.3 km higher than  
221 the mean precipitation. Compared with NC, radar reflectivity within convective overshooting over SC  
222 and MEC are stronger and their DPDH feature are more similar. Their echo top height is ~18 km, 6.5 km  
223 higher than total precipitation, 4.5 km higher than NC, and their echo near surface concentrated around  
224 30-55 dBZ, while that of total precipitation is between 15 dBZ and 43 dBZ. Besides, Radar reflectivity of





225 convective overshooting over NC accounts for a higher proportion below the zero level, while MEC and  
226 SC account for a higher proportion above the zero level, which indicate that the upward motion within  
227 convective overshooting over MEC and SC are stronger and there are more ice crystal particles.

228 Quantitative analysis of the vertical structure of precipitation within convective overshooting is one of  
229 the main issues of interest to this study. Shown as Fig. 7, the rain rate profiles of convective overshooting  
230 are provided, and to highlight its unique feature, rain rate profiles of total precipitation and convective  
231 precipitation are also given. In general, the rain rate of convective overshooting is very higher, especially  
232 below the zero level (~5 km), 5-10 times than normal precipitation, indicating stronger convection and a  
233 greater precipitation of ice. In addition, differences between three regions are obvious. Rain rate of  
234 convective overshooting over NC is about twice lower than MEC and SC, which is consistent with the  
235 results of radar echo. At 1 km altitude, rain rate of convective overshooting are 12 mm/h (NC), 22.5  
236 mm/h (MEC), and 23 mm/h (SC) respectively. Below zero level, the variation of rain rate with altitude is  
237 not very obvious, and difference of rain rate between convective overshooting and normal precipitation  
238 are ~8 mm over NC and ~20 mm over MEC and SC. Above zero level, rain rate of convective  
239 overshooting decreases obviously with altitude increasing, and rain rate are 6mm/h (NC), 10 mm (MEC)  
240 and 6.5mm (SC) at 10 km. However, rain rate of other precipitation are no more than 2 mm/h above 8 km,  
241 we therefore suggest that the strong upward flow within convective overshooting brings large amounts of  
242 moisture from the lower layer to the upper layer.

243 We conduct the Probability Density Function (PDF) analysis on the Near Surface Rain Rate (NSRR)  
244 within convective overshooting, and that of total and convective precipitation are also calculated, shown  
245 as Fig. 8. Grade of precipitation are as follows: Light rain: <4.9 mm/12 h, Moderate rain: 5.0-14.9  
246 mm/12h, Heavy rain: 15.0-29.9 mm/12h, Torrential rain: 30.0-69.9 mm/12h, Downpour: 70.0-139.9  
247 mm/12h, and Heavy downpour: ≥140.0 mm/12h (General Administration of Quality Supervision, 2012).

248 The PDF curve of NSRR of convective overshooting is obviously different from normal precipitation,  
249 and has regional differences. The peak value of PDF of convective overshooting appears at ~10 mm/h,  
250 belonging to downpour, however, that of normal precipitation appear at ~1 mm/h, belonging to moderate  
251 rain, which is obviously lower than convective overshooting. And the PDF of peak value of convective  
252 overshooting over NC is about 11.5%, while that over MEC and SC are about 6%. Besides, sample size  
253 of convective overshooting with precipitation grade of heavy downpour account for 34.0% (NC), 46.7%  
254 (MEC) and 34.8% (SC) respectively, 3-10 times than normal precipitation, which remind us to pay



255 special attention to the extreme precipitation events caused by convective overshooting that may cause  
256 harm to our production and life.

### 257 3.2.3 Microphysical features

258 GPM center provides particle spectrum from dual-frequency radar. Based on the DSD profiles from  
259 2ADPR, we further investigate the microphysical structures of convective overshooting. The Liquid  
260 Water Path (LWP) and Ice Water Path (IWP) show the overall water content in the atmospheric column,  
261 which is closely associated with microphysical processes within convective overshooting. To quantify  
262 the characteristics of LWP and IWP within convective overshooting, the PDF of LWP and IWP of  
263 convective overshooting are shown as Fig. 9, and that of convective and total precipitation are also  
264 shown for comparison. The LWP and IWP within convective overshooting are the highest, with high  
265 value of PDF mainly distributed around  $1000 \text{ g/m}^3$  and  $5000 \text{ g/m}^3$  respectively, much higher than that of  
266 normal precipitation, which are around  $100 \text{ g/m}^3$  and  $300 \text{ g/m}^3$ , indicating sufficient water vapor inside  
267 convective overshooting. And differences of IWP between convective overshooting and normal  
268 precipitation are bigger than LWP, suggesting that differences of water vapor above zero level between  
269 them is greater and convective overshooting brings water vapor from bottom of the troposphere to higher  
270 layers. Besides, differences of LWP and IWP between three regions are also worth noting: The LWP and  
271 IWP over MEC and SC are more similar and higher than NC. Especially, LWP over MEC has a bimodal  
272 structure with peaks of  $630$  and  $5000 \text{ g/m}^3$ , which are consistent with the bimodal structure of NSRR  
273 PDF curve in Fig. 8. Analysis above in Fig. 1b shows that tropopause height over northern MEC is lower  
274 than southern MEC, making convective overshooting easier happen over northern MEC, which indicates  
275 that there are two types of convective overshooting events over MEC, weak events with lower storm top  
276 height and strong events with higher storm top height, which correspond to the two peaks of LWP PDF  
277 curve respectively.

278 We further use DSD parameter profiles, including the effective radius ( $D_0$ ) and droplet concentration  
279 ( $\text{dBN}_0$ ) profiles, to analyze the microphysical characteristics within convective overshooting, shown as  
280 Fig. 10. Results show that the microphysical processes within convective overshooting are unique,  
281 leading to various properties of the droplets in precipitation. Droplets of convective overshooting are  
282 large, but sparse. Influenced by strong updrafts, precipitation particles within convective overshooting  
283 continuously collide and grow large enough to fall, therefore, the effective radius of droplets are big,



284 below 10 km altitude, almost exceeding 2.5 mm, which is about twice than that of normal precipitation.  
285 However, the droplet concentration within convective overshooting is relatively lower. Differences of  
286 microphysical structure between three regions are also worth noting. Convective overshooting events  
287 over NC have large, but sparse droplets, while that over SC have small, but dense droplets, and the  
288 effective radius and concentration of droplets over MEC are between NC and SC, which is speculated  
289 that it's related to the differences of aerosol content and types over three regions. Specifically, at 1 km  
290 altitude, the effective radius of droplets over NC is the largest (2.87 mm), followed by MEC (2.7 mm),  
291 and SC is the lowest (2.5 mm). As altitude increases, the effective radius of droplets first increase and  
292 then decrease, with maximum of 2.93 mm over NC at 2.5 km and sharp peak over MEC (2.85 mm) and  
293 SC (2.76 mm) near zero level, about twice than normal precipitation. The effective radius of droplets for  
294 convective overshooting over NC and MEC are lower than 2.5 mm above 10 km and 12 km respectively.  
295 It's worth noting that the effective radius of droplets for convective overshooting over SC show an  
296 increasing trend above 8 km altitude, which are similar to convective precipitation, and their effective  
297 radius of droplets over three regions also show an increasing tend from 9 km to 13 km, which may be  
298 related to the strong upward motion inside. When the upward motion is strong, ice particles must grow  
299 large enough to fall (Langmuir, 1948). Droplet concentration basically decreases with altitude, and that  
300 within convective overshooting is obviously lower than normal precipitation and NC is the lowest, while  
301 MEC and SC are higher and similar. Droplet concentration within convective overshooting near ground  
302 is the highest, with NC (25.4), MEC (28) and SC (28), while that of normal precipitation is mainly  
303 distributed between 32 and 35.

304 Convective overshooting plays an important role in exchanging constituents and energy between  
305 troposphere and stratosphere. To quantify its impact, temperature, humidity, vertical velocity, and ozone  
306 profiles from ERA5 are used to further analyze the internal thermodynamic characteristics of convective  
307 overshooting and their impacts on atmospheric composition. The atmospheric temperature (Fig. 11aei)  
308 and absolute humidity profiles within convective overshooting are statistically analyzed (Fig. 11bfj), and  
309 the difference profiles between them with the total atmospheric profiles are shown as Fig.12ab. The  
310 atmospheric temperature has a wavy response to convective overshooting, and the response varies in  
311 different regions. Warming and cooling effect caused by convective overshooting over NC is the most  
312 obvious compared with MEC and SC, no more than 1K. Near surface, convective overshooting exhibits  
313 warming effect, that over NC is 2 K, and that over MEC and SC are no more than 1 K. From surface to ~2



314 km altitude, warming effect caused by convective overshooting over three regions gradually decreased.  
315 From 5 km to the middle tropopause height, convective overshooting shows cooling effect over NC, with  
316 sharp peak -4 K at 11.5 km altitude. Near tropopause, convective overshooting show warming effect over  
317 NC and MEC, and the most warming effect over NC can reach 4 K at 16.5 km altitude; Convective  
318 overshooting has an obvious humidifying effect on the air below the cloud top, with humidifying MEC  
319 most and NC least. The humidification effect caused by convective overshooting first increases and then  
320 decreases, with maximum of  $2.3 \text{ g/m}^3$  (MEC),  $1.45 \text{ g/m}^3$  (SC) and  $0.8 \text{ g/m}^3$  (NC) at 1 km altitude.  
321 To further explore dynamic structure characteristics within convective overshooting and its effect on  
322 ozone, we calculated the vertical velocity profiles (Fig. 11c) and ozone profiles (Fig. 11d) within  
323 convective overshooting. And the difference profiles between them with the total atmospheric profiles  
324 are shown as Fig. 12. Results show that upward motion within convective overshooting is very strong,  
325 the upward motion over MEC is the strongest, followed by SC and NC, and that over SC is slightly  
326 higher than NC. From surface to middle tropopause, the upward motion within convective overshooting  
327 firstly becomes stronger and then weakens. The vertical velocity over MEC can reach a maximum of  
328  $-0.85 \text{ Pa/s}$  at 6 km altitude. The vertical velocity over SC is about  $-0.35 \text{ Pa/s}$  from 6 km to 11.5 km. The  
329 highest vertical velocity over NC is  $-0.3 \text{ Pa/s}$  at 6.5 km. At the bottom of the stratosphere, there is a slight  
330 downward movement of air, which is because the mixture of strong divergent flow and turbulence  
331 mechanically drags the air above the clouds outward, and the air above the clouds are pulled down due to  
332 continuity.  
333 The impact of convective overshooting on ozone can be divided into three parts: Below 10 km (middle  
334 and lower troposphere), convective overshooting makes ozone mass mixing ratio slightly decrease, with  
335 decrease no more than  $0.03 \times 10^{-6} \text{ kg/kg}$ ; From 10 km to 26 km (upper and middle troposphere and lower  
336 stratosphere), convective overshooting obviously increases ozone mass mixing ratio. The increase of  
337 ozone mass mixing ratio caused by convective overshooting over NC is the highest, with sharp peak  
338  $0.3 \times 10^{-6} \text{ kg/kg}$  at 19 km, followed by MEC, with sharp peak  $0.25 \times 10^{-6} \text{ kg/kg}$  at 19 km, and SC is the  
339 lowest, with sharp peak  $\sim 0.1 \times 10^{-6} \text{ kg/kg}$  from 21 to 25 km; Above 26 km, ozone mass mixing ratio  
340 decreases obviously caused by convective overshooting, with the maximum of  $0.24 \times 10^{-6} \text{ kg/kg}$ . The  
341 most obvious change of ozone mass mixing ratio caused by convective overshooting is the increase of  
342 ozone at tropopause and lower stratosphere, which is partly due to the strong upward motion within  
343 convective overshooting (Fig. 12) causing the influx of ozone from lower troposphere. On the other



344 hand, it's due to the sinking of air with high concentration ozone in the stratosphere, and the descent  
345 vertical velocity at the bottom of the stratosphere also confirms this (Fig. 12c).

#### 346 **4 Summary and conclusions**

347 The microphysical characteristics of convective overshooting are essential but poorly understood due to  
348 the difficulty in accurately detecting the convective overshooting and obtaining microphysical  
349 parameters during severe weather events. Based on the microphysical precipitation data from GPM DPR  
350 and the meteorological data from ERA5 data, we designed a more accurate algorithm for convective  
351 overshooting determination and examine the particle size, concentration, phase state and other  
352 parameters of the convective overshooting over East China. The main conclusions are:

353 Firstly, the horizontal distribution characteristics of convective overshooting over East China are  
354 analysed by designing a more accurate algorithm for convective overshooting determination. Statistical  
355 results indicate that the frequency of the convective overshooting over East China is very low, with a  
356 magnitude of only  $10^{-3}$ , with large regional differences. Convective overshooting events occur obviously  
357 more frequently over NC and northern MEC, than SC and southern MEC, mainly because of the lower  
358 tropopause height of the former and the different underlying surfaces. The mean convective overshooting  
359 storm top height mostly ranges from 10 km to 21 km and has obvious regional distribution differences.  
360 And convective overshooting storm top height over NC is 5-6 km higher than SC.

361 Based on the reflectivity profiles and the rain-rate profiles provided by the GPM DPR instrument, we  
362 studied the vertical structure of precipitation within convective overshooting. The DPDH analysis of the  
363 radar reflectivity shows that radar reflectivity within convective overshooting is obviously stronger and  
364 its storm top height is higher. And the DPDH analysis also shows obviously regional differences. Radar  
365 reflectivity of convective overshooting over NC accounts for a higher proportion below the zero level,  
366 while MEC and SC account for a higher proportion above the zero level, which indicate that the upward  
367 motion within convective overshooting over MEC and SC are stronger and there are more ice crystal  
368 particles. Rain rate results also show that rain rate within convective overshooting is higher, 5-10 times  
369 than that of normal precipitation. Especially, sample number of strong precipitation with grade of  
370 precipitation of heavy downpour accounts for 34.0% (NC), 46.7% (MEC), and 34.8% (SC), which  
371 remind us to pay special attention to the extreme precipitation events caused by convective overshooting.



372 GPM center provides particle spectrum from dual-frequency radar. Based on the DSD profiles from  
373 2ADPR, we further investigated the microphysical structures of convective overshooting. Statistical  
374 results show that convective overshooting has unique microphysical characteristics compared with  
375 normal precipitation, with obvious regional differences. The LWP and IWP within convective  
376 overshooting are abundant, with high values of PDF distributed around  $1000 \text{ g/m}^3$  and  $5000 \text{ g/m}^3$   
377 respectively. Moreover, influenced by strong updrafts, precipitation particles within convective  
378 overshooting continuously collide and grow large enough to fall, therefore, the effective radius is big,  
379 below 10 km altitude, almost exceeding 2.5 mm, which is about twice than that of normal precipitation.  
380 However, the droplet concentration within convective overshooting is relatively lower. Differences of  
381 microphysical structure between three regions are also worth noting. The effective radius of droplet over  
382 NC is slightly bigger than MEC and SC, while the droplet concentration is lower, which is speculated  
383 that it's related to the differences of aerosol content and types over three regions.

384 Convective overshooting plays an important role in exchanging constituents and energy between  
385 troposphere and stratosphere. To quantify its impact, temperature, humidity, vertical velocity, and ozone  
386 profiles from ERA5 are used to further analyse the internal thermodynamic characteristics of convective  
387 overshooting and their impacts on atmospheric composition. The atmospheric temperature has a wavy  
388 response to convective overshooting, and the response varies in different regions. Convective  
389 overshooting has an obvious humidifying effect on the atmosphere below the cloud top, with  
390 humidifying MEC most and NC least. The upward motion within convective overshooting is very strong,  
391 and the order of the ascending velocity between three regions corresponds to the order of their  
392 humidifying effects, which also reflects that the humidifying effect of convective overshooting is related  
393 to internal dynamics, consistent with study of Chae et al. (2011). In addition, convective overshooting  
394 events not only bring ozone from lower troposphere to upper troposphere and lower stratosphere, but also  
395 sink air with high concentration ozone in the stratosphere, thereby reducing the ozone in the stratosphere  
396 and lower troposphere, and obviously increasing the ozone in the upper troposphere and lower  
397 stratosphere.

398 Quantitative study of the internal microphysical characteristics within convective overshooting has not  
399 been documented previously. Findings of this study may have important implications for the  
400 microphysical evolution associated with convective overshooting, and provide more accurate  
401 precipitation microphysical parameters as the input of the model simulation. This study is the



402 continuation of the previous research (Sun et al., 2021). In the future, we will further explore the impact  
403 of aerosol on the internal microphysical characteristics within convective overshooting, and more  
404 microphysical parameters with higher spatiotemporal resolution are expected to provide more detailed  
405 features.

406 **Data availability.** ERA5 data are taken from  
407 <https://www.ecmwf.int/en/forecasts/datasets/reanalysis-datasets/era5>. GPM DPR data are archived at  
408 <https://gpm.nasa.gov/data/directory>.

409 **Acknowledgements.** This work was funded by the National Natural Science Foundation of China  
410 Project (Grant No. 42230612) and the fellowship of China Postdoctoral Science Foundation (Grant  
411 Numbers: 2022M723011).

412 **Author contributions.** Sun N., Lu G.P., and Fu Y.F. framed up this study. All the authors discussed the  
413 concepts. Sun N. conducted the data analyses. Sun N. drafted the manuscript and all authors edited the  
414 manuscript.

415 **Competing interests.** The authors declare no competing interests.

## 416 References

417 Anderson, J. G., Wilmouth, D. M., Smith, J. B. and Sayres, D. S.: UV dosage levels in summer:  
418 Increased risk of ozone loss from convectively injected water vapor, *Science*, 337, 835-839,  
419 <https://doi.org/10.1126/science.1222978>, 2012.

420 Avery, M. A., Davis, S. M., Rosenlof, K. H., Ye, H. and Dessler, A. E.: Large anomalies in lower  
421 stratospheric water vapour and ice during the 2015–2016 El Niño, *Nature Geoscience*, 10, 405-409,  
422 <https://doi.org/10.1038/ngeo2961>, 2017.

423 Alcalá, C. M. and Dessler, A. E.: Observations of deep convection in the tropics using the Tropical  
424 Rainfall Measuring Mission (TRMM) precipitation radar, *Journal of Geophysical Research:  
425 Atmospheres*, 107, 4792, <https://doi.org/10.1029/2002JD002457>, 2002.

426 Biondi, R., Randel, W. J., Ho, S. P., Neubert, T. and Syndergaard, S.: Thermal structure of intense  
427 convective clouds derived from GPS radio occultations, *Atmospheric Chemistry and Physics*, 12,  
428 5309-5318, <https://doi.org/10.5194/acp-12-5309-2012>, 2012.



- 429 Bedka, K., Murillo, E. M., Homeyer, C. R., Scarino, B. and Mersiowsky, H.: The above-anvil cirrus  
430 plume: An important severe weather indicator in visible and infrared satellite imagery, *Weather and*  
431 *Forecasting*, 33, 1159-1181, <https://doi.org/10.1175/WAF-D-18-0040.1>, 2018.
- 432 Chaboureau, J. P., Cammas, J. P., Duron, J., Mascart, P. J., Sitnikov, N. M. and Voessing, H. J.: A  
433 numerical study of tropical cross-tropopause transport by convective overshoots, *Atmospheric*  
434 *Chemistry and Physics*, 7, 1731-1740, <https://doi.org/10.5194/acp-7-1731-2007>, 2007.
- 435 Corti, T., Luo, B. P. and De Reus, M. et al.: Unprecedented evidence for deep convection hydrating the  
436 tropical stratosphere, *Geophysical Research Letters*, 35, L10810,  
437 <https://doi.org/10.1029/2008GL033641>, 2008.
- 438 Chemel, C., Russo, M. R., Pyle, J. A., Sokhi, R. S. and Schiller, C.: Quantifying the imprint of a severe  
439 hector thunderstorm during ACTIVE/SCOUT-O3 onto the water content in the upper  
440 troposphere/lower stratosphere, *Monthly weather review*, 137, 2493-2514,  
441 <https://doi.org/10.1175/2008MWR2666.1>, 2009.
- 442 Chae, J. H., Wu, D. L., Read, W. G. and Sherwood, S. C.: The role of tropical deep convective clouds on  
443 temperature, water vapor, and dehydration in the tropical tropopause layer (TTL), *Atmospheric*  
444 *Chemistry and Physics*, 11, 3811-3821, <https://doi.org/10.5194/acp-11-3811-2011>, 2011.
- 445 Danielsen, E. F.: In situ evidence of rapid, vertical, irreversible transport of lower tropospheric air into  
446 the lower tropical stratosphere by convective cloud turrets and by larger - scale upwelling in tropical  
447 cyclones, *Journal of Geophysical Research: Atmospheres*, 98, 8665-8681,  
448 <https://doi.org/10.1029/92JD02954>, 1993.
- 449 De Reus, M., Borrmann, S. and Bansemmer, A. et al: Evidence for ice particles in the tropical stratosphere  
450 from in-situ measurements, *Atmospheric Chemistry and Physics*, 9, 6775-6792,  
451 <https://doi.org/10.5194/acp-9-6775-2009>, 2009.
- 452 Fueglistaler, S., Wernli, H. and Peter, T.: Tropical troposphere - to - stratosphere transport inferred from  
453 trajectory calculations, *Journal of Geophysical Research: Atmospheres*, 109, D03108,  
454 <https://doi.org/10.1029/2003JD004069>, 2004.
- 455 Frey, W., Schofield, R. and Hoor, P. et al.: The impact of overshooting deep convection on local  
456 transport and mixing in the tropical upper troposphere/lower stratosphere (UTLS), *Atmospheric*  
457 *Chemistry and Physics*, 15, 6467-6486, <https://doi.org/10.5194/acp-15-6467-2015>, 2015.





- 458 General Administration of Quality Supervision, Inspection and Quarantine of the People's Republic of  
459 China: Standardization Administration of the People's Republic of China, GB/T 28592—2012 Grade  
460 of precipitation, Standards Press of China, 2012.
- 461 Grosvenor, D. P., Choulaton, T. W., Coe, H. and Held, G.: A study of the effect of overshooting deep  
462 convection on the water content of the TTL and lower stratosphere from Cloud Resolving Model  
463 simulations, *Atmospheric Chemistry and Physics*, 7, 4977-5002,  
464 <https://doi.org/10.5194/acp-7-4977-2007>, 2007.
- 465 Gettelman, A., Salby, M. L. and Sassi, F.: Distribution and influence of convection in the tropical  
466 tropopause region, *Journal of Geophysical Research: Atmospheres*, 107, 4080,  
467 <https://doi.org/10.1029/2001JD001048>, 2002.
- 468 Homeyer, C. R. and Kumjian, M. R.: Microphysical characteristics of overshooting convection from  
469 polarimetric radar observations, *Journal of the Atmospheric Sciences*, 72, 870-891,  
470 <https://doi.org/10.1175/JAS-D-13-0388.1>, 2015.
- 471 Hoffmann, L., Günther, G. and Li, D. et al.: From ERA-Interim to ERA5: the considerable impact of  
472 ECMWF's next-generation reanalysis on Lagrangian transport simulations, *Atmospheric Chemistry  
473 and Physics*, 19, 3097-3124, <https://doi.org/10.5194/acp-19-3097-2019>, 2019.
- 474 Highwood, E. J. and Hoskins, B. J.: The tropical tropopause, *Quarterly Journal of the Royal  
475 Meteorological Society*, 124, 1579-1604, <https://doi.org/10.1002/qj.49712454911>, 1998.
- 476 Jensen, E. J., Ackerman, A. S. and Smith, J. A.: Can overshooting convection dehydrate the tropical  
477 tropopause layer?, *Journal of Geophysical Research: Atmospheres*, 112, D11209,  
478 <https://doi.org/10.1029/2006JD007943>, 2007.
- 479 Johnston, B. R., Xie, F. and Liu, C.: The effects of deep convection on regional temperature structure in  
480 the tropical upper troposphere and lower stratosphere, *Journal of Geophysical Research:  
481 Atmospheres*, 123, 1585-1603, <https://doi.org/10.1002/2017JD027120>, 2018.
- 482 Khaykin, S., Pommereau, J. P. and Korshunov, L. et al.: Hydration of the lower stratosphere by ice  
483 crystal geysers over land convective systems, *Atmospheric Chemistry and Physics*, 9, 2275-2287,  
484 <https://doi.org/10.5194/acp-9-2275-2009>, 2009.
- 485 Langmuir, I.: The production of rain by a chain reaction in cumulus clouds at temperatures above  
486 freezing, *Journal of the Atmospheric Sciences*, 5(5), 175-192,  
487 [https://doi.org/10.1175/1520-0469\(1948\)005<0175:TPORBA>2.0.CO;2](https://doi.org/10.1175/1520-0469(1948)005<0175:TPORBA>2.0.CO;2), 1948.



- 488 Liu, N. and Liu, C.: Global distribution of deep convection reaching tropopause in 1 year GPM  
489 observations, *Journal of Geophysical Research: Atmospheres*, 121, 3824-3842,  
490 <https://doi.org/10.1002/2015JD024430>, 2016.
- 491 Liu, N., Liu, C. and Hayden, L.: Climatology and detection of overshooting convection from 4 years of  
492 GPM precipitation radar and passive microwave observations, *Journal of Geophysical Research:*  
493 *Atmospheres*, 125, e2019JD032003, <https://doi.org/10.1029/2019JD032003>, 2020.
- 494 Liu, C. and Zipser, E. J.: Global distribution of convection penetrating the tropical tropopause, *Journal of*  
495 *Geophysical Research: Atmospheres*, 110, D23104, <https://doi.org/10.1029/2005JD006063>, 2005.
- 496 Liu, P., Wang, Y., Feng, S., Li, C. Y. and Fu, Y. F.: Climatological characteristics of overshooting  
497 convective precipitation in summer and winter over the tropical and subtropical regions, *Chin. J.*  
498 *Atmos. Sci.*, 36, 579-589, <https://doi.org/10.3878/j.issn.1006-9895.2011.11109>, 2012.
- 499 Line, W. E., Schmit, T. J., Lindsey, D. T. and Goodman, S. J.: Use of geostationary super rapid scan  
500 satellite imagery by the Storm Prediction Center, *Weather and Forecasting*, 31, 483-494,  
501 <https://doi.org/10.1175/WAF-D-15-0135.1>, 2016.
- 502 Machado, L. A. T., Rossow, W. B., Guedes, R. L. and Walker, A. W.: Life cycle variations of mesoscale  
503 convective systems over the Americas, *Monthly Weather Review*, 126, 1630-1654,  
504 [https://doi.org/10.1175/1520-0493\(1998\)126<1630:LCVOMC>2.0.CO;2](https://doi.org/10.1175/1520-0493(1998)126<1630:LCVOMC>2.0.CO;2), 1998.
- 505 Muhsin, M., Sunilkumar, S. V., Ratnam, M. V., Parameswaran, K., Murthy, B. K. and Emmanuel, M.:  
506 Effect of convection on the thermal structure of the troposphere and lower stratosphere including the  
507 tropical tropopause layer in the South Asian monsoon region, *Journal of Atmospheric and*  
508 *Solar-Terrestrial Physics*, 169, 52-65, <https://doi.org/10.1016/j.jastp.2018.01.016>, 2018.
- 509 Marion, G. R., Trapp, R. J. and Nesbitt, S. W.: Using overshooting top area to discriminate potential for  
510 large, intense tornadoes, *Geophysical Research Letters*, 46, 12520-12526,  
511 <https://doi.org/10.1029/2019GL084099>, 2019.
- 512 Rodriguez - Franco, J. J. and Cuevas, E.: Characteristics of the subtropical tropopause region based on  
513 long - term highly resolved sonde records over Tenerife, *Journal of Geophysical Research:*  
514 *Atmospheres*, 118, 10-754, <https://doi.org/10.1002/jgrd.50839>, 2013.
- 515 Rossow, W. B. and Pearl, C.: 22 - year survey of tropical convection penetrating into the lower  
516 stratosphere, *Geophysical research letters*, 34, L04803, <https://doi.org/10.1029/2006GL028635>,  
517 2007.



- 518 Solomon, S., Rosenlof, K. H. and Portmann, R. W. et al.: Contributions of stratospheric water vapor to  
519 decadal changes in the rate of global warming, *Science*, 327, 1219-1223,  
520 <https://doi.org/10.1126/science.1182488>, 2010.
- 521 Sherwood, S. C. and Dessler, A. E.: A model for transport across the tropical tropopause, *Journal of the*  
522 *Atmospheric Sciences*, 58, 765-779,  
523 [https://doi.org/10.1175/1520-0469\(2001\)058<0765:AMFTAT>2.0.CO;2](https://doi.org/10.1175/1520-0469(2001)058<0765:AMFTAT>2.0.CO;2), 2001.
- 524 Sun, N., Fu, Y., Zhong, L., Zhao, C. and Li, R.: The Impact of Convective Overshooting on the Thermal  
525 Structure over the Tibetan Plateau in Summer Based on TRMM, COSMIC, Radiosonde, and  
526 Reanalysis Data, *Journal of Climate*, 34, 8047-8063, <https://doi.org/10.1175/JCLI-D-20-0849.1>,  
527 2021.
- 528 Sun, N., Fu, Y., Zhong, L. and Li, R.: Aerosol effects on the vertical structure of precipitation in East  
529 China, *npj Climate and Atmospheric Science*, 5, 60, <https://doi.org/10.1038/s41612-022-00284-0>,  
530 2022a.
- 531 Sun, N., Zhong, L., Zhao, C., Ma, M. and Fu, Y.: Temperature, water vapor and tropopause  
532 characteristics over the Tibetan Plateau in summer based on the COSMIC, ERA-5 and IGRA datasets,  
533 *Atmospheric Research*, 266, 105955, <https://doi.org/10.1016/j.atmosres.2021.105955>, 2022b.
- 534 Sherwood, S. C., Horinouchi, T. and Zeleznik, H. A.: Convective impact on temperatures observed near  
535 the tropical tropopause, *Journal of Atmospheric Sciences*, 60, 1847-1856,  
536 [https://doi.org/10.1175/1520-0469\(2003\)060<1847:CIOTON>2.0.CO;2](https://doi.org/10.1175/1520-0469(2003)060<1847:CIOTON>2.0.CO;2), 2003.
- 537 Takahashi, H. and Luo, Z. J.: Characterizing tropical overshooting deep convection from joint analysis of  
538 CloudSat and geostationary satellite observations, *Journal of Geophysical Research: Atmospheres*,  
539 119, 112-121, <https://doi.org/10.1002/2013JD020972>, 2014.
- 540 World Meteorological Organization.: Meteorology—A three - dimensional science: Second session of  
541 the commission for aerology, *WMO Bull*, 4, 134-138, 1957.
- 542 Xu, W.: Thunderstorm climatologies and their relationships to total and extreme precipitation in China,  
543 *Journal of Geophysical Research: Atmospheres*: 125, e2020JD033152,  
544 <https://doi.org/10.1029/2020JD033152>, 2020.
- 545 Yuter, S. E. and Houze, R. A.: Three-dimensional kinematic and microphysical evolution of Florida  
546 cumulonimbus. Part II: Frequency distributions of vertical velocity, reflectivity, and differential



547 reflectivity, Monthly Weather Review, 123(7), 1941-1963,  
548 [https://doi.org/10.1175/1520-0493\(1995\)123<1941:TDKAME>2.0.CO;2](https://doi.org/10.1175/1520-0493(1995)123<1941:TDKAME>2.0.CO;2), 1995.

549 Zhang, A. and Fu, Y.: Life cycle effects on the vertical structure of precipitation in East China measured  
550 by Himawari-8 and GPM DPR, Monthly Weather Review, 146, 2183-2199,  
551 <https://doi.org/10.1175/MWR-D-18-0085.1>, 2018.

552

553

554

555

556

557

558

559

560

561

562

563

564

565

566

567

568

569

570



571 **Tables**

572 **Table1.** The sample number of total precipitation, convective precipitation, and convective overshooting over NC,  
573 MEC, and SC.

574

Sample number (count, ct)	NC	MEC	SC
Total Precipitation	652489	546313	319127
Convective Precipitation	111903	137674	111900
Convective Overshooting	2394	582	296

575

576

577

578

579

580

581

582

583

584

585

586

587

588

589

590

591

592

593

594

595

596

597

598

599

600

601

602

603

604

605

606

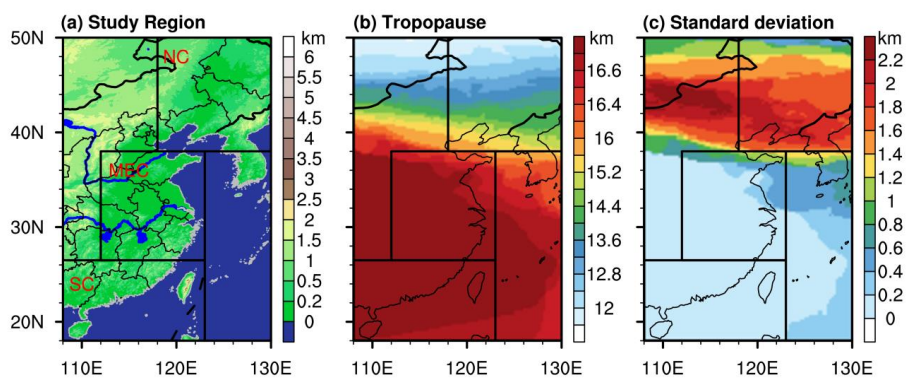
607

608

609

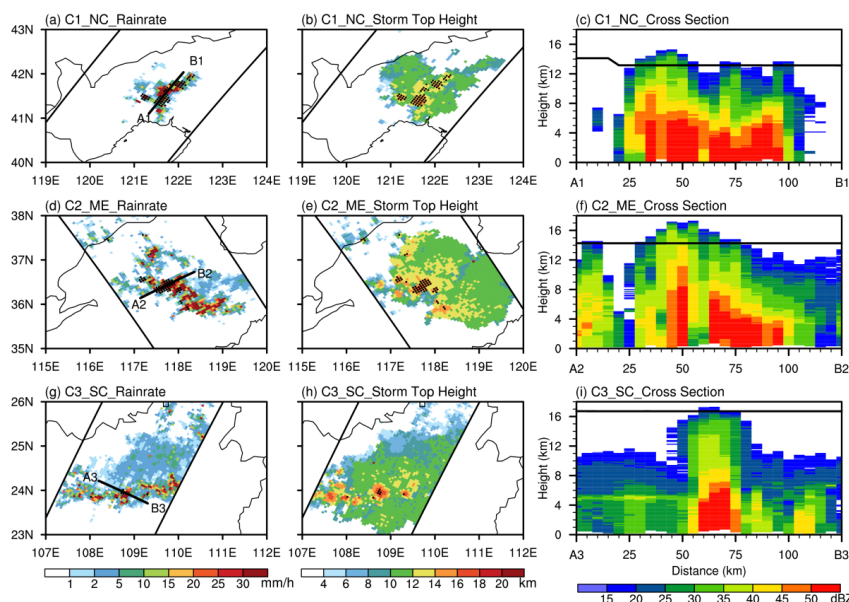


610 **Figures**



611

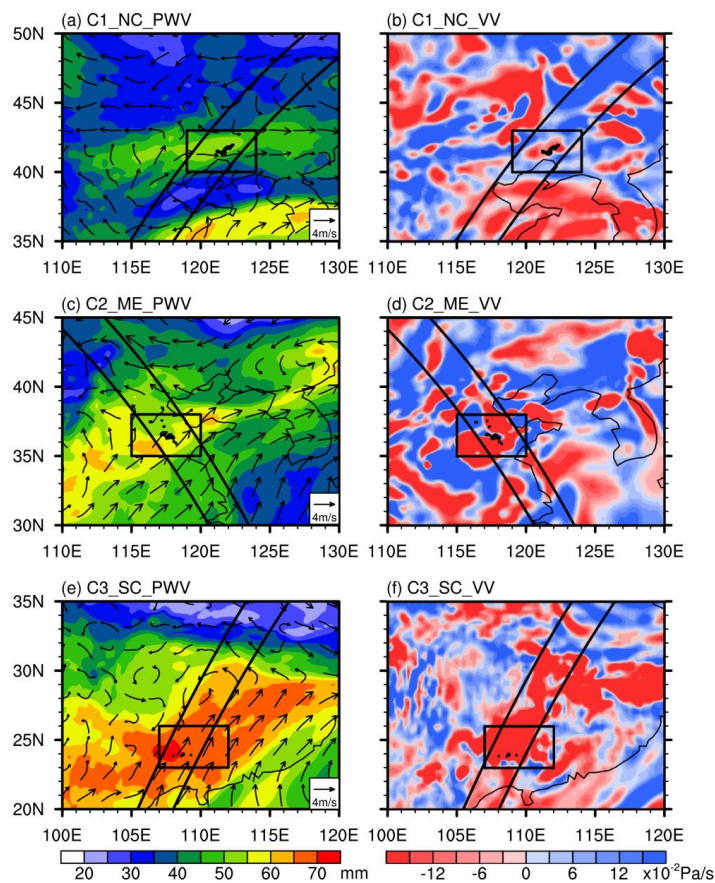
612 **Figure 1.** Study areas and their tropopause characteristics. (a) Regionalization of East China (Black boxes:  
613 Divisions between NC, MEC and SC, and only the land surface is studied) and their terrain features. (b)  
614 Distribution of tropopause height. (c) Distribution of standard deviation of tropopause height.



615

616 **Figure 2.** Precipitation characteristics of convective overshooting cases. **(a)** Distribution of rain rate of Case 1 (C1)  
617 and the occurrence time of C1 is at 14:00 on July 1, 2017. (The pixels in which convective overshooting occurs are  
618 marked as black boxes). **(b)** Distribution of storm top height of C1. **(c)** Radar reflectivity cross section along A1B1  
619 and the black line show the tropopause height along A1B1. **(d)** Distribution of rain rate of C2 and the occurrence  
620 time of C2 is at 13:00 on July 30, 2015. **(e)** Distribution of storm top height of C2. **(f)** Radar reflectivity cross  
621 section along A2B2. **(g)** Distribution of rain rate of C3 and the occurrence time of C3 is at 17:00 on June 13, 2015.  
622 **(h)** Distribution of storm top height of C3. **(i)** Radar reflectivity cross section along A3B3.

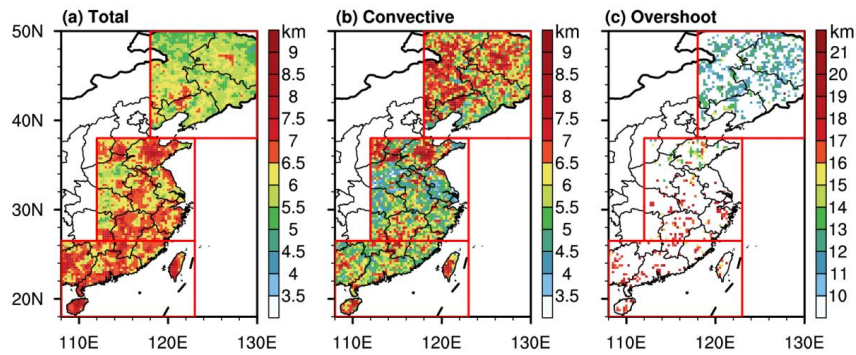
623



624  
625 **Figure 3.** Characteristics of large scale circulation of convective overshooting cases. (a) Distribution of  
626 precipitable water vapor (PWV) and streamlines at 850 hPa of C1. The area where the case occurred is marked as  
627 big black boxes and the pixels in which convective overshooting occurs are marked as little black boxes. The black  
628 line is the GPM detection orbit. (b) Distribution of vertical velocity (VV) at 500 hPa of C1. (c) Distribution of  
629 PWV and streamlines of C2. (d) Distribution of VV of C2. (e) Distribution of PWV and streamlines of C3. (f)  
630 Distribution of VV of C3.

631  
632





633

634 **Figure 4.** Geographical distribution of storm top height. (a) Distribution of storm top height for total precipitation.

635 (b) Distribution of storm top height for convective precipitation. (c) Distribution of storm top height for convective

636 overshooting.

637

638

639

640

641

642

643

644

645

646

647

648

649

650

651

652

653

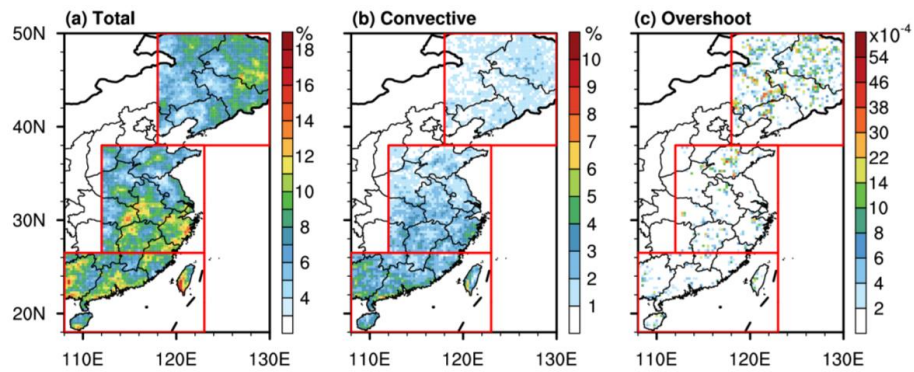
654

655

656

657

658



659

660 **Figure 5.** Precipitation frequency. (a) Frequency of total precipitation. (b) Frequency of convective precipitation.  
661 (c) Frequency of convective overshooting.

662

663

664

665

666

667

668

669

670

671

672

673

674

675

676

677

678

679

680

681

682

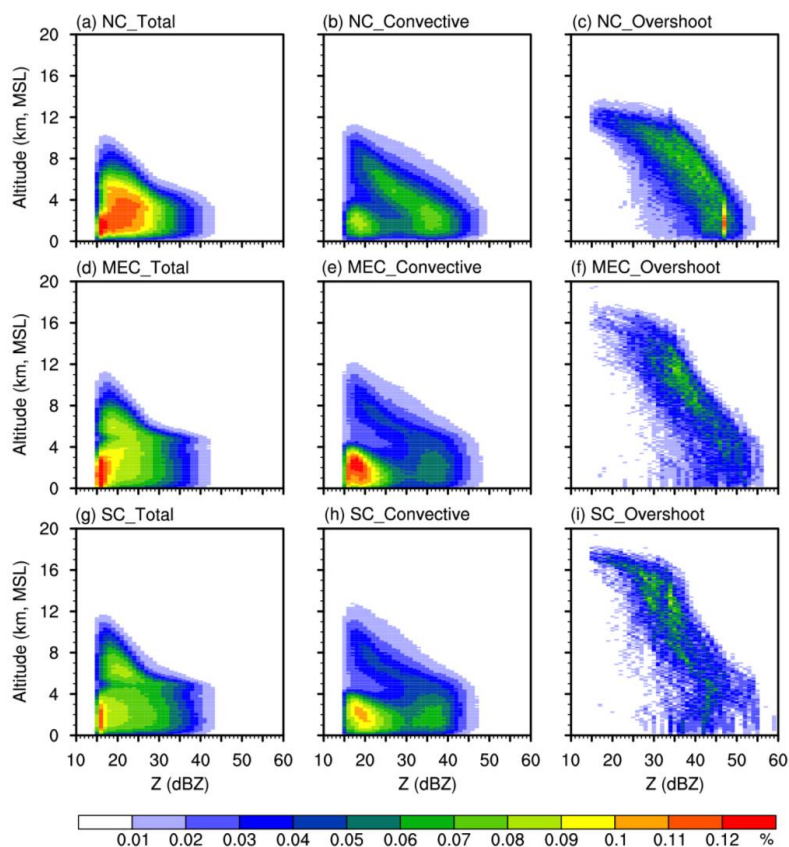
683

684

685

686

687



688

689 **Figure 6.** DPDH (Distribution of Probability Density with Height) of radar reflectivity. (a) DPDH for total  
690 precipitation over NC. (b) DPDH for convective precipitation over NC. (c) DPDH for convective overshooting  
691 over NC. (d) DPDH for total precipitation over MEC. (e) DPDH for convective precipitation over MEC. (f) DPDH  
692 for convective overshooting over MEC. (g) DPDH for total precipitation over SC. (h) DPDH for convective  
693 precipitation over SC. (i) DPDH for convective overshooting over SC.

694

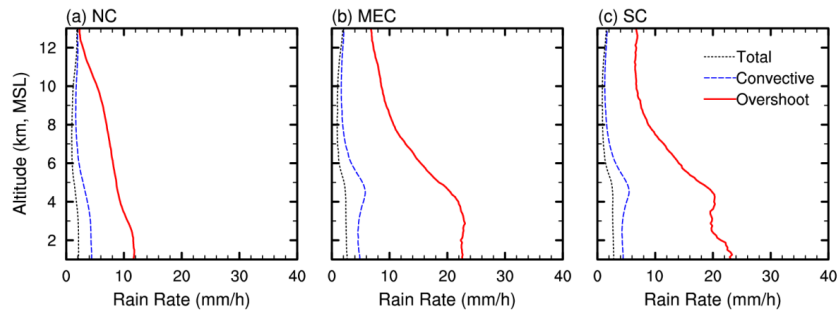
695

696

697

698

699



700

701 **Figure 7.** Rain rate profiles for total precipitation, convective precipitation and convective overshooting (Red lines  
702 are convective overshooting; Blue lines are the convective precipitation; Black lines are the total precipitation). (a)  
703 The rain rate profiles over NC. (b) The rain rate profiles over MEC. (c) The rain rate profiles over SC.

704

705

706

707

708

709

710

711

712

713

714

715

716

717

718

719

720

721

722

723

724

725

726

727

728

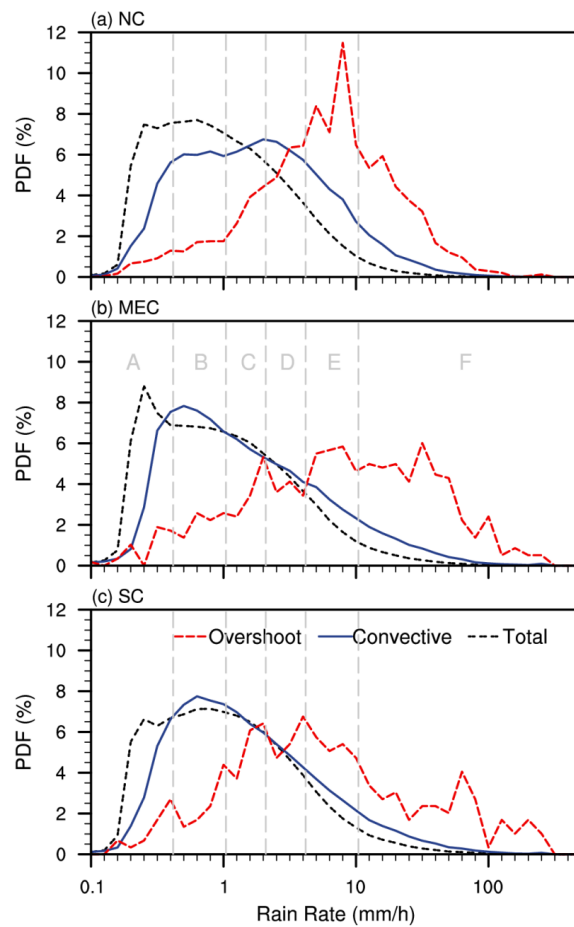
729

730

731

732

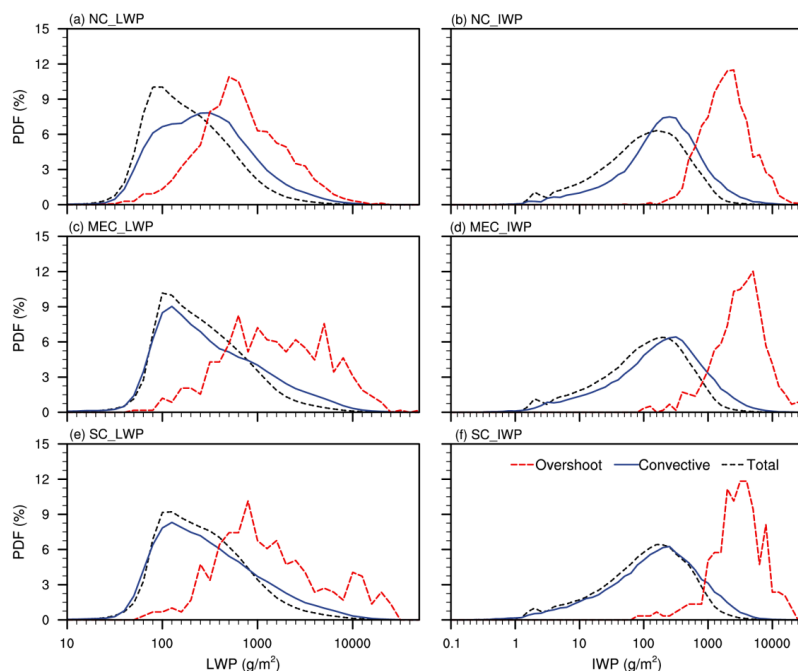
733



734

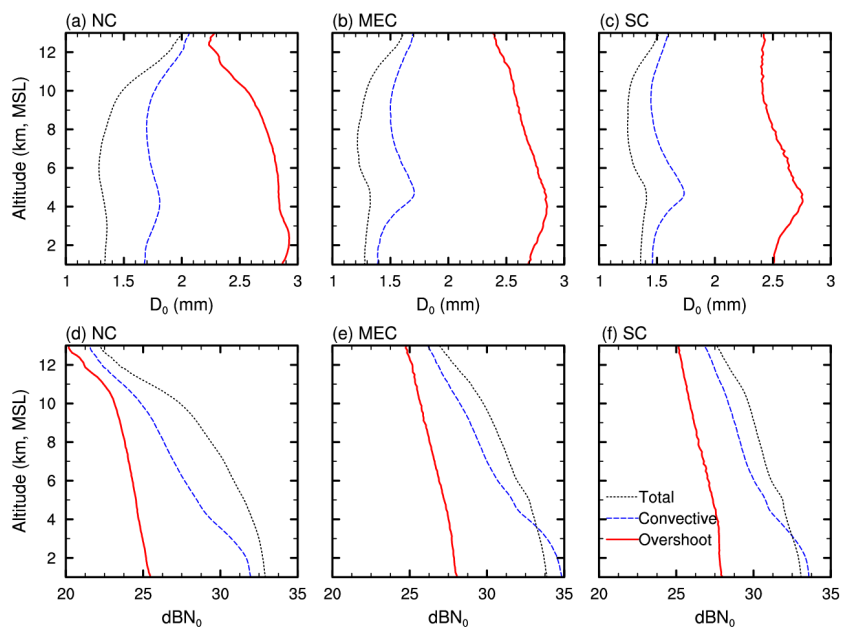
735 **Figure 8.** Probability Density Function (PDF) of Near Surface Rain Rate (NSRR). (a) PDF of NSRR in NC. (b)

736 PDF of NSRR in MEC. (c) PDF of NSRR in SC.



737  
738  
739  
740  
741  
742  
743  
744  
745  
746  
747  
748  
749  
750  
751  
752  
753  
754  
755  
756

**Figure 9.** PDF of Liquid Water Path (LWP) and Ice Water Path (IWP). (a) PDF of LWP over NC. (b) PDF of IWP over NC. (c) PDF of LWP over MEC. (d) PDF of IWP over MEC. (e) PDF of LWP over SC. (f) PDF of IWP over SC.



757

758

759

760

761

762

763

764

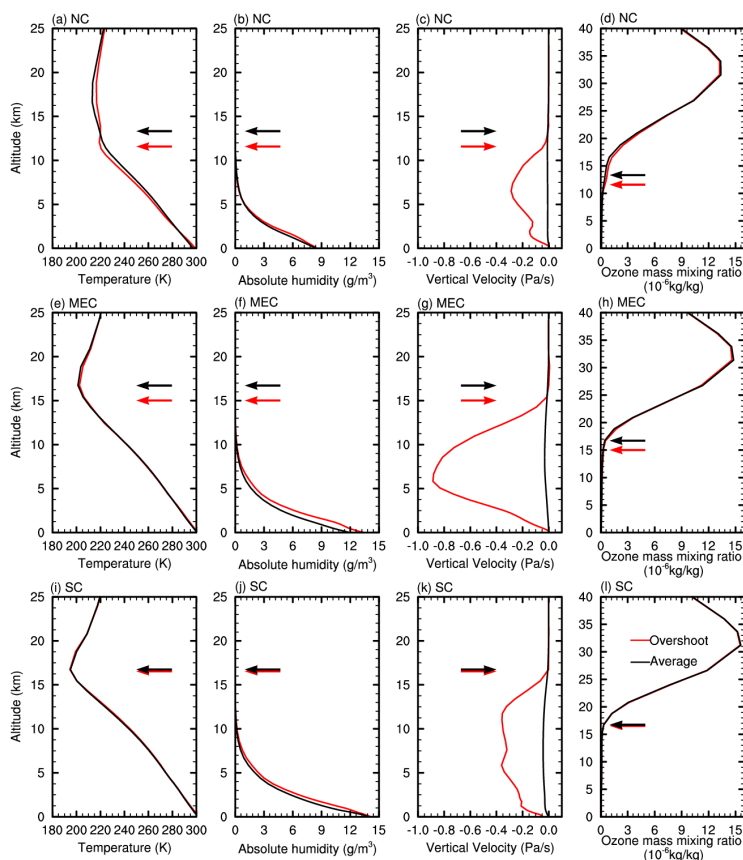
765

766

767

768

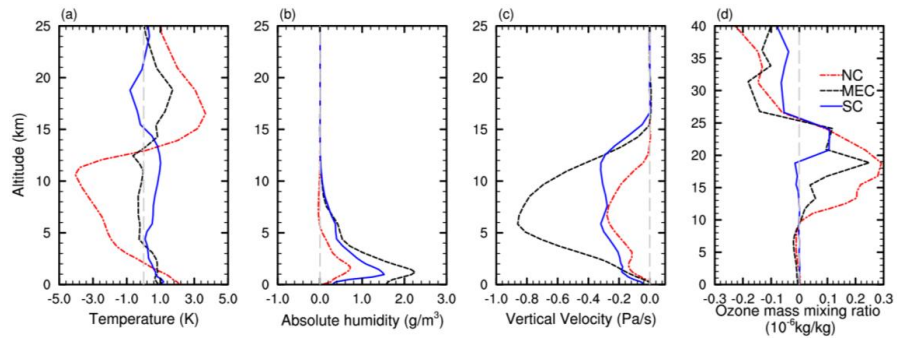
**Figure 10.** The droplet concentration ( $dBN_0$ ) and effective radius ( $D_0$ ) profiles for total precipitation, convective precipitation and convective overshooting over NC, MEC and SC. **(a)** The  $dBN_0$  profiles over NC. **(b)** The  $dBN_0$  profiles over MEC. **(c)** The  $dBN_0$  profiles over SC. **(d)**  $D_0$  profiles over NC. **(e)**  $D_0$  profiles over MEC. **(f)**  $D_0$  profiles over SC.



769  
 770 **Figure 11.** Atmospheric parameter profiles for total precipitation and convective overshooting over NC, MEC and  
 771 SC. (a) Temperature profiles over NC. (b) Absolute humidity profiles over NC. (c) Vertical velocity profiles over  
 772 NC. (d) Ozone mass mixing ratio profiles over NC. (e) Temperature profiles over MEC. (f) Absolute humidity  
 773 profiles over MEC. (g) Vertical velocity profiles over MEC. (h) Ozone mass mixing ratio profiles over MEC. (i)  
 774 Temperature profiles over SC. (j) Absolute humidity profiles over SC. (k) Vertical velocity profiles over SC. (l)  
 775 Ozone mass mixing ratio profiles over SC.

776  
 777  
 778





779  
780 **Figure 12.** Difference of atmospheric parameters profiles between total precipitation and convective overshooting  
781 over NC, MEC and SC. **(a)** Difference of temperature profiles. **(b)** Difference of absolute humidity profiles. **(c)**  
782 Difference vertical velocity profiles.

783  
784  
785  
  
786  
  
787  
  
788